



Experimental characterisation of the spreading of polymeric powders in powder bed fusion additive manufacturing process at changing temperature conditions

Sina Zinatlou Ajabshir ^{a,b}, Daniele Sofia ^{a,1}, Colin Hare ^b, Diego Barletta ^a, Massimo Poletto ^{a,*}

^a Department of Industrial Engineering, University of Salerno, Italy

^b School of Engineering, Newcastle University, Newcastle upon Tyne NE1 7RU, UK

ARTICLE INFO

Article history:

Received 22 November 2023

Received in revised form 1 March 2024

Accepted 22 March 2024

Keywords:

Powder Bed Fusion

Laser Beam

Spreadability

Powder layer quality

Powder flow behaviour

High temperature

ABSTRACT

This study investigates the spreadability behaviour of four different polymeric materials, namely Polyamide 6, Polyamide 6 Black, Polypropylene, and Thermoplastic Polyurethane, under different spreading speeds (30 and 3 mm/s) and powder bed temperatures (25, 80, 110 °C) using a purposely developed experimental apparatus. Macroscopic and microscopic images of the powder layer were taken after completing the powder spreading step. A thresholding-based image processing method was utilised to evaluate the fraction of the bed area not covered by particles (NCF), and the standard deviation of pixel intensities in grayscale images (SDG) was calculated to evaluate powder layer quality in macroscopic images. NCF and SDG can provide quantitative evaluation of the quality of the spread layer, NCF in a logarithmic scale ranking and SDG in a linear scale ranking. A wavelet analysis technique was developed on microscopic panorama images obtained with grazing light to characterise the surface roughness of the layer. Results indicate that the spreadability generally worsens much more significantly than powder flow properties at increasing temperatures and, remarkably, that flowability and spreadability are unrelated. As expected, the temperature effect on powder spreading changes for the different powders are mostly governed by the approach to the powder melting temperature. Minor effects on the final layer quality were also observed at changing spreading speed.

© 2024 Published by Elsevier B.V. on behalf of The Society of Powder Technology Japan. All rights reserved.

1. Introduction

Powder bed Fusion (PBF) is one of the additive manufacturing (AM) techniques classified by ISO/ASTM 52900. It involves selectively fusing and bonding specific areas of a powdered material bed to create 3D objects by Laser Beam (LB) [1–4]. One of the Powder Bed Fusion techniques with LB (PBF-LB abbreviated based on the standard [1]) is called Selective Laser Sintering (SLS), and Deckard was the first to introduce it [5–7]. While many SLS machines either partially or completely melt the materials they work with, it is worth noting that the term “sintering” is a historical label and not entirely accurate. In fact, the process usually entails either full or partial melting, rather than the traditional method of powdered sintering [1]. In PBF-LB, the primary powder feedstock is

delivered in layers from the fresh powder resource. A LB is used as the heat source to fuse the powder layer selectively (Fig. 1). Powder feedstocks in PBF-LB can be metallic [8–12], ceramic [13–15], polymeric [16–20] or any blend of those materials [21–25]. In the PBF-LB method, the movement of the LB is digitally operated, often starting from a CAD input. The three-dimensional fabricated components are completed by alternating the formation of new powder layers and selective fusing on each layer in an iterative process.

The properties of powders used in the PBF-LB process should be adequate and satisfy the handleability and operability of the procedure. One of the powder properties that can affect the quality of PBF-LB products is the flow behaviour under process conditions. Better powder flowability improves the quality of the formed powder bed and the final product [26–28]. However, powder flowability may not coincide with powder spreadability [29–31], or more precisely, the powder spreadability in the PBF-LB process can depend on 1) the physical properties of the powder particles, such as shape [29,32], size [33,34], and interparticle forces [35–37], as

* Corresponding author.

E-mail address: mpoletto@unisa.it (M. Poletto).

¹ Presently at Dipartimento di Ingegneria Informatica, Modellistica, Elettronica e Sistemistica of the Università della Calabria.

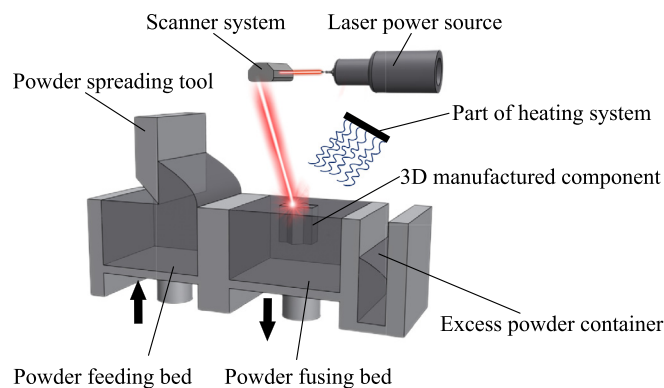


Fig. 1. Schematic view of the Powder Bed Fusion with Laser Beam (PBF-LB).

well as 2) the operation and environmental parameters, including the powder and environmental humidity [28], the powder bed temperature [37,38], and the powder spreading tool shape [39,40] and speed [31,40]. The bed temperature in PBF-LB is affected by the preheating phase in the fusing bed (Fig. 1), which is performed for its benefits [41–49], such as the improved quality of the produced solid materials [50,51]. The reduced thermal stresses [44,46] minimise crack formation, residual stresses and artefact deformation due to the reduced thermal gradients [42,44–48,52,53]. In addition, it would increase the final component density due to the enhanced wetting of the fused phase [54,55] obtained by supplying sufficient heat input [43]. Besides, using higher bed temperatures in the process decreases the laser energy demand for fusing [56]. Unfortunately, the powder preheating can reduce the powder flowability, leading to worse spreadability and impairing the powder bed preparation strategy [35,36,57–59]. Therefore, assessing the suitability of the powder materials for their use in the PBF-LB process requires understanding the effect of the temperature on spreadability to identify the best operating conditions.

The quality of the spread powder bed is related to the evenness and homogeneity of the powder layer, which should have no unfilled spots.

Various methods are available to evaluate the quality of the spread powder bed, including layer mass analysis, which measures the weight of the powder layer to estimate its density [28,30,60]. Although mass analysis is a convenient and efficient technique for assessing the quality of a spread powder bed, it may not provide the level of precision required for certain applications. The mass analysis technique can identify regions with insufficient or excessive powder but does not provide details on the layer's thickness, uniformity, or surface characteristics. More advanced techniques, such as surface roughness analysis, may be used to assess the quality of the spread powder bed. Several limitations have been identified in the literature regarding evaluating the spreading process parameters, including the adoption of specific devices, such as a customised commercial roughness-measuring instrument, to be used during the spreading stage, which requires complex procedures to be used that may not be compatible with in situ measurements on large samples [26,32]. Few studies have focused on developing simple and easy-to-use methods for analysing the quality of the powder layer, which could limit the ability of researchers and manufacturers to optimise the powder bed manufacturing process. Such methods could include techniques such as optical microscopy, profilometry, or digital image analysis, which offer a non-destructive and cost-effective means of assessing powder layer quality [61–63]. Furthermore, several studies have evaluated

the surface quality of powder beds at ambient temperature, particularly in terms of surface roughness and uniformity [31,64], and the impact of higher temperatures on powder surface quality has been assessed regarding the onset of apparent defects of the bed surface [38]. There is a need for additional research to better understand the impact of temperature on the quality of the powder layer even below the onset of macroscopic defects.

The present work aims to quantitatively assess the surface quality of polymeric powder beds obtained by spreading at elevated temperatures in a dedicated experimental setup. In particular, the surface roughness of powder layers is measured by means of image analysis techniques both at the macroscopic and microscopic scales. The spreading results are also compared with the powders' flowability obtained by shear testing at different temperatures.

2. Materials and methods

2.1. Powder and particle physical properties

Four engineered polymeric powders purposely designed for PBF-LB application with various melting temperatures (T_m) were used in this work. Two types of Polyamide powders were included: Polyamide 6 (PA6) and Ultrasint[®] Low Melting Polyamide 6 (PA6 black). Polyamide PA6 powder is developed by SINTERLINE[®] for PBF-LB. Polyamide PA6 black powder is developed by BASF 3D Printing Solutions GmbH. It has a black colour and a lower melting temperature than PA6. The other two powders used are Ultrasint[®] Polypropylene (PPNAT, BASF 3D Printing Solutions GmbH), designed as a substitute for Polyamide for PBF-LB, and Ultrasint[®] Thermoplastic polyurethane (TPU, BASF 3D Printing Solutions GmbH) powder, which is produced to print very fine structures with a high level of detail.

2.1.1. Particle size distribution

Particle Size Distribution (PSD) analysis was carried out using the Malvern Instruments-Laser diffraction method based on Mie theory with water dispersant (Mastersizer Hydro 2000S, Malvern, UK).

The PSD results of all materials are represented in detail in Fig. 2. The width of the distribution curve is quantified by the span, which is the difference between the particle size at 90% and 10% of the cumulative undersize distribution normalised by the median of the particle size distribution. Smaller span values indicate narrower distribution curves. According to Fig. 2, PA6 black and PPNAT show a slightly narrower PSD span than PA6 and TPU. Moreover, TPU has the largest mean diameter (d_{50}), 82 μm , and PA6 has the smallest mean diameter, 46 μm . The mean diameter of PA6 black and PPNAT are 74 μm and 69 μm , respectively. Further information on these powders is given in Table 1.

2.1.2. Morphology and particle shape

A morphology and shape observation was done employing a scanning electron microscope (SEM) (FESEM, mod. LEO 1525, Carl Zeiss SMT AG, Oberkochen, Germany). Differential scanning calorimetry (DSC) test was accomplished from 50 $^{\circ}\text{C}$ to 225 $^{\circ}\text{C}$ at 10 $^{\circ}\text{C}/\text{min}$ heating stage under nitrogen gas with 20 ml/min heat flow to find out any physical transformation of the powders during the high-temperature tests by Diamond TG/DTA.

The SEM images in Fig. 3 represent the particle shape (panes a, b, d, e, g, h, j and k) and surface texture (panes c, f, i and l) of the materials under investigation. The images reveal that the particles exhibit irregular rather than completely rounded shapes. Specifically, elongated and angular particles are observed in PA6 powders in Fig. 3a and b. TPU powder appears polyhedral with

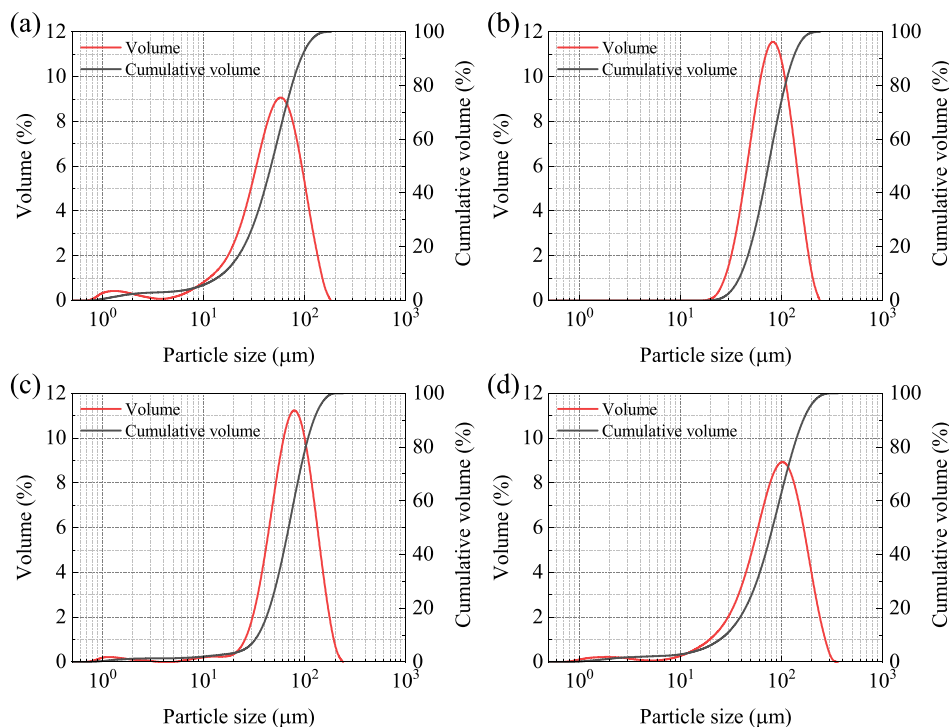


Fig. 2. Particle size distribution results: (a) PA6; (b) PA6 black; (c) PPNAT; and (d) TPU (red lines provide frequencies of particle size occurrence in bins characterised by a ratio between the maximum and minimum particle size of 1.182).

Table 1
Powders properties. Span is $(d_{90} - d_{10})/d_{50}$ and SSA is the Specific Surface Area.

Materials	$T_{melting}(^{\circ}C)$	$\rho_B(kg/m^3)$	$\rho_p(kg/m^3)$	$d_{10}(\mu m)$	$d_{50}(\mu m)$	$d_{90}(\mu m)$	$d_{2.3}(\mu m)$	$d_{3.4}(\mu m)$	span	SSA(m^2/g)
PA6	210	525	1130	15	46	91	20	50	1.65	0.303
PA6 black	193	590	1370	40	74	129	66	80	1.20	0.0907
PPNAT	140	330	890	35	69	122	36	74	1.26	0.168
TPU	120–150	500	1100	28	82	163	35	90	1.64	0.173

multi-dimensional shapes and sharp-edged particles in Fig. 3j and 3 k. In contrast, PA6 black and PPNAT powders exhibit approximately oval-shaped particles in Fig. 3d, e, g, and h.

SEM images show that the surface of particles of PA6 (Fig. 3c) and TPU (Fig. 3l) powders are characterised by a surface texture showing some finer particle dust covering their surfaces. On the other hand, the particle surfaces of PA6 black and PPNAT powders are characterised by pores and delaminating material (Fig. 3f) and a few cracks (Fig. 3h and i).

The irregular particle shape and rough surface texture can affect the particles' flow, packing, and adhesion, which in turn can impact the performance of the materials in the spreading process [62,65].

2.1.3. Thermal analysis

Thermal analysis was carried out to investigate any significant physical transformation of materials in the range of testing temperatures. The investigated temperature range of Differential Scanning Calorimetry (DSC) in the heating phase was from 50 °C to 225 °C. Inspection of DSC thermograms in Fig. 4 indicates PA6, PA6 black, PPNAT, and TPU only responded to the temperature at their melting point with an endothermic peak at 210 °C, 190 °C, 140 °C and 135 °C respectively. Other than the above, there are no further transformations in these materials. Sharp and well-defined melting peaks correspond to greater crystallinity within their semi-crystalline structure.

2.2. Powder shear testing

Powder shear testing was carried out with the Anton Paar MCR 302 WESP to evaluate the flowability of powders under different consolidation states and temperatures. The Anton Paar apparatus is equipped with an oven which heats the sample inside the shear cell up to 500 °C and keeps the temperature constant during the test. The procedure was started by filling the cell with dried powder and levelling it. Then, the lid was moved close to the powder surface. After that, the heating system was closed to start the pre-heating steps. 15–25 min intervals were adopted to equalise the temperature. Afterwards, preshear and shear steps were done to measure the powder flow function with specified normal stress during preshear at 1, 2, 4 and 8 kPa. Flow function measurements were repeated at temperatures ranging from ambient to values approaching the powder melting point.

2.3. Powder spread testing

The powder spreading test was performed in an apparatus developed by the Powder Technology group at the University of Salerno [31]. This device mimics the spreading stage of commercial PBF-LB machines. In this work, a heating chamber was designed and built to heat the powder beds, the spreading metal plate and the spreading tool (blade-shaped) to the desired temperatures

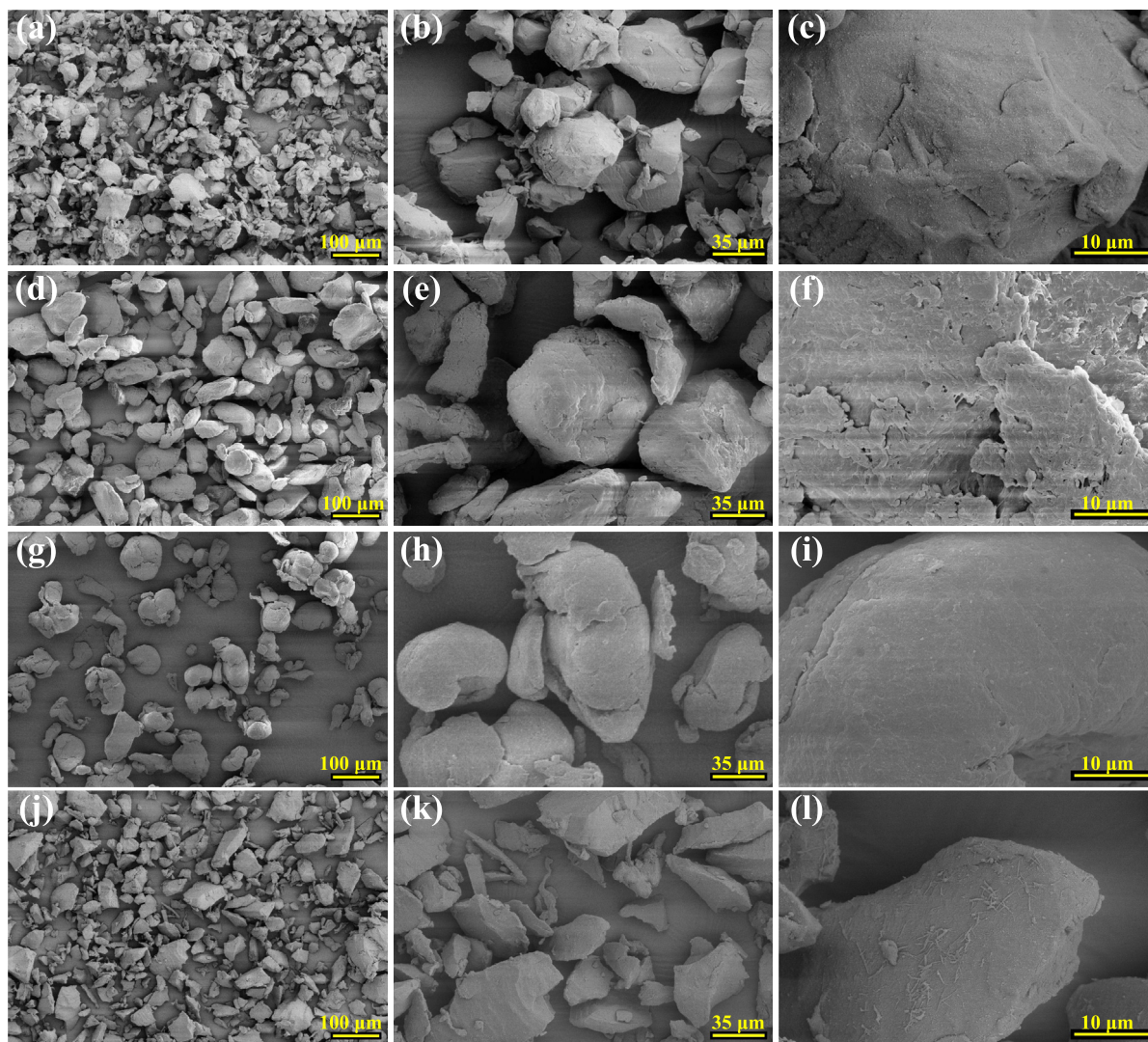


Fig. 3. SEM images of powders at various magnifications: (a)-(c) PA6; (d)-(f) PA6 black; (g)-(i) PPNAT, and (j)-(l) TPU.

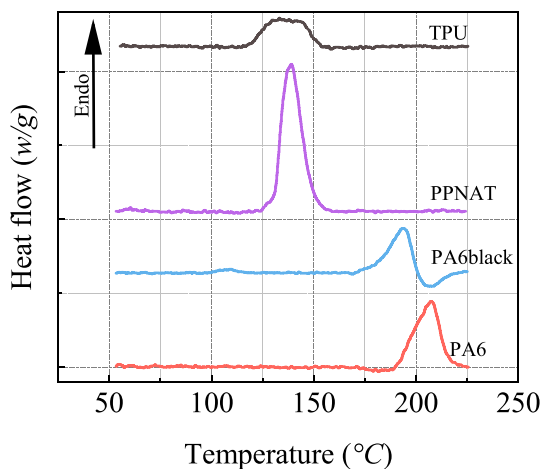


Fig. 4. DSC thermograms of polymeric powders in the heating stage from 50 °C up to 225 °C.

(Fig. 5). The heat sources are two different types of heaters working simultaneously. An IR Lamp above the powder bed heats the powder beds directly through radiation. Two electrical resistance heaters

keep the temperature uniform inside the heating chamber, acting mainly by convection.

The steps of the spreading process are shown in Fig. 6. As shown in Fig. 6f, the metal spreading plate hosts two 10 × 10 cm square shape trays with 300 μm depth. A depth of 300 μm is more than twice the d_{90} value for all the powders tested. This depth avoids particle jamming phenomena, possibly worsened by spreading over a rigid tray bottom rather than another powder layer [61]. Furthermore, the value of 300 μm comfortably falls within the recommended range for layer thickness in PBF-LB, which should ideally be at least twice the average size of the particles. This ensures that powder fusion predominantly happens through direct contact of the laser with individual particles rather than relying solely on particle-to-particle conduction, particularly in the case of polymeric powders [66,67]. The first and second trays in the spreading direction are named feeding bed and fusing bed, respectively.

The experimental procedure mimicking the spreading process at temperature includes different phases. The first is the preparation of the feeding bed, the second is the heating and spreading phase, and the third is the bed analysis phase. The second phase includes the main spreading step, which is carried out to spread powder from the feeding bed to the fusing bed.

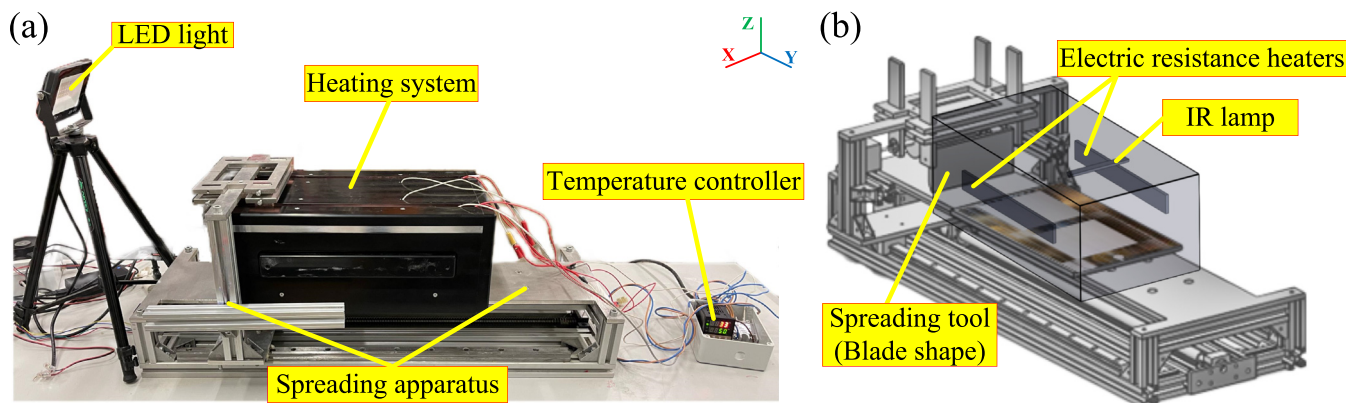


Fig. 5. Powder spreading apparatus covered by the heating system: (a) device picture and (b) schematic overview of the device.

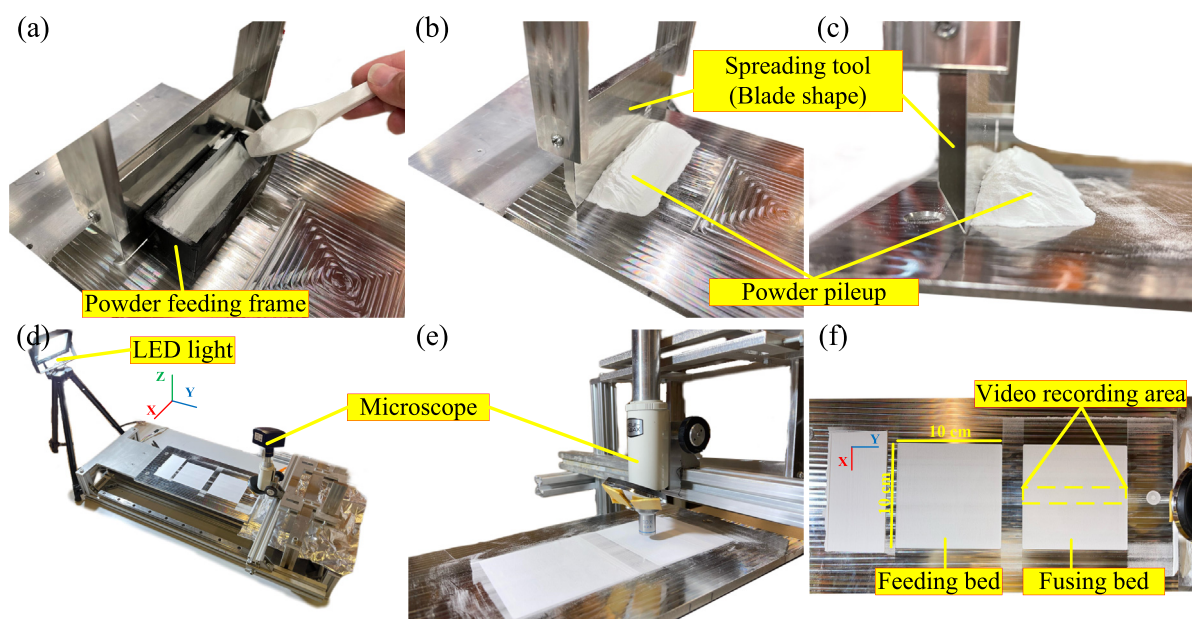


Fig. 6. Various steps of the spreading process: (a) powder loading; (b) powder pileup in front of the blade; (c) side-view of spreading tool and powder pileup; (d) birds-eye view of the device after spreading; (e) microscope location, and (f) top-view of powder beds in the spreading device.

In detail, the phase dedicated to preparing the feeding bed starts with drying the powder at 110 °C for 1 h. Then, the powder was sieved to break any potential agglomerates formed while drying. The blade-shaped spreading tool in the spreading device was located 5 cm before the feeding bed, with the edge at 1 mm above the spreading plate. The powder was poured with a spoon in front of the blade using a rectangular frame (100 × 30 × 30 mm) to shape the pile (Fig. 6a). After lifting this frame, a powder pile was formed in front of the blade, ready to use. Then, the blade was started, and the formed powder pileup in front of the blade was delivered to the feeding bed (Fig. 6b and c). The extra powder around the feeding bed was removed, and the blade was returned to its starting position, where the blade height was reduced to leave an almost zero gap between the edge and the metal plate. The feeding bed with a height of 1.3 mm powder has been prepared and is now ready for heating and spreading.

In the second phase, the heating system was assembled, and the powder bed and the rest of the metal plate were heated up. Reaching the desired temperature and allowing some time for the temperature equalisation of the chamber, the spreading tool (blade-shaped) was set in motion to take the powder from the feeding

bed and generate a new powder layer with 300 μm depth in the fusing bed. Finally, the heating chamber is removed, uncovering the prepared bed for the quality analysis (Fig. 6d).

The powder bed temperature and spreading speed were considered variables in the spreading process. Three temperatures, 25, 80, and 110 °C, and two spreading speeds, 30 and 3 mm/s, were studied. The speed of 30 mm/s is the largest possible with the laboratory setup, and the speed of 3 mm/s was assumed to introduce a significant change in the parameter. These speeds are somewhat smaller than the typical spreading speeds adopted in commercial equipment. Modifying the apparatus to reach these speed values is in the present plans and will be the objective of future studies. At each temperature, both speed conditions were considered. Three repetitions for each state were done. The temperature equalisation time was 20 min at 80 °C and 30 min at 110 °C.

2.4. Image analysis

For the bed quality analysis phase, a lamp was placed in front of the prepared bed so that the light would hit the powder bed surface at 45° from the horizontal (Fig. 6d).

2.4.1. Macroscopic image analysis

For visual and macroscopic inspection, a camera (iPhone 14 Pro max 48 MP f/1.8, 24 mm) placed perpendicular to the prepared powder bed captured the top view of the fusing bed (Fig. 6f). Image analysis methods were employed to provide a quantitative evaluation of the spread powder layer's quality. Images were first converted from colour images into grayscale images to calculate the standard deviation of the grey level (SDG) in the image pixels. It is assumed that in images of layers fully covering the tray, wider variations of the grey level within the image can be associated with deeper valleys and higher crests, highlighted by the grazing light. Even larger variations of pixels' grey level should be determined in correspondence to layer defects leaving the powder bed surface uncovered.

Then, binarised images were obtained, adopting a threshold adequate to distinguish between the dark tray background and the brighter powder. This procedure allows a straightforward estimation of the bed area fraction that is irregularly or not covered by the powder (NCF). Of course, this procedure was possible only with bright material and could not be carried out for PA6 black. The threshold values able to correctly discriminate between the background pixels and the darker powder layer pixels for bright powders (PA6, PPNAT, and TPU) was determined to be 130 over a range of possible grey levels between 0 (black) and 255 (white). The threshold value of 130 was chosen after a visual comparison between different binarised images and the original, as it appeared to correctly include all the areas not covered with particles. Furthermore, the chosen threshold appeared to fall in the bimodal histograms of the grey level distribution in the fairly wide region between the peak of the whites of the powder layer and the peak of the blacks of the uncovered areas. Therefore, the final result of the binarising operation with this threshold value was rather independent of slight changes in specific image illumination of the originals, which could determine a slight shift of the histogram.

2.4.2. Microscopic image analysis

For microscopic and quantitative analysis, a microscopic imaging digital camera (AmScope MU1603 16 MP USB3.0) mounting a 10X lens of a microscope was used. It was fixed on the mobile bridge in place of the blade. The vertical position of the camera setup was adjusted for focus, and the lateral position was adjusted according to the analysis needs. The camera was generally away from the border of the powder bed to avoid wall effects (Fig. 6e). A sequence of frames of the bed surface was taken and stored while the camera moved along the spreading direction. The recorded videos were also converted to panorama strip view images that covered the first 15 mm of the fusing powder bed along the spreading direction for a width of 1.1 mm.

The analysis procedure defined by Lupo et al. [31] was adopted. Light intensity values of pixels were extracted from lines crossing the panorama strips in the spreading direction. Three positions of these lines were considered: one along the strip axis and two closer to the strip side. To stabilise the signal derived from these series, in each position along the spreading direction, the light intensity was averaged between the light intensity taken from 3 adjacent pixels orthogonal to the spreading direction. These signals were processed with the Matlab tool for wavelet analysis. Wavelet power spectra (PS) allowed for identifying the characteristic dimension of the powder surface roughness. The wavelength of the peak of the PS was named as a peak length (pl). This parameter helps to estimate surface quality by observing changes in the location of pl along the wavelengths. It can be supposed that a shift in the peak length value towards a lower wavenumber (higher wavelength) in the averaged power spectra indicates a larger characteristic length of the surface, which, in turn, represents a lower surface quality. The objective was to obtain useful information about the quality

of the powder layer at the particle scale after its distribution with the spreading tool. Adopting this approach allowed for finding characteristic lengths indicating the bed surface quality for each powder, spreading speed, and powder bed temperature. Further details about wavelet analysis are given in a previous work [31].

3. Results

3.1. Flow functions

Shear test results are presented in terms of flow functions, which are the unconfined yield stress values, f_c , reported as a function of the major principal stress, σ_1 , applied during consolidation. In order to classify the flow behaviour of materials at the specific temperature and consolidation stress, the Jenike flowability categorisation was considered. It is reproduced by the dashed lines in Fig. 7 representing the limiting flow factor values $ff = \sigma_1/f_c$ between the Jenike classes reported in italics in the figure. Higher values of the flow factor correspond to better flowability. In the order of decreasing flowability, the classes are free-flowing, easy-flowing, cohesive, very cohesive and hardened (not flowing).

According to Fig. 7a, the flowability of PA6 at 25 °C, 110 °C and 130 °C falls in the range of free-flowing powders at all consolidation stresses even though f_c gradually increases with temperature. At 170 °C, the flow factor of PA6 is found in the range of easy flowing powders. At 190 °C, the flow factor of PA6 rises to the cohesive range, particularly at higher consolidation stresses. By approaching the melting temperature at 195 °C and 200 °C (0.93 T_m and 0.95 T_m respectively), the flow factor of PA6 shows a further marked rise in the cohesive range, almost reaching the very cohesive range.

Fig. 7b shows that the flow factor of PA6 black is in the free flowing range at 25 °C and 120 °C, while it is between the free flowing and easy flowing ranges at 155 °C. The slight temperature increment to 160 °C leads to flowability in the easy flowing range at all tested stresses. The flow factor of PA6 black peaked at 170 °C and fell into the cohesive range.

The flow factor of PPNAT powder (Fig. 7c) falls within the free flowing and easy flowing ranges at 25 °C and 115 °C, respectively. It is within the cohesive range at 127 °C and 131 °C.

Fig. 7d indicates that TPU has a free-flowing behaviour at 25 °C like all tested polymers. It exhibits a slight rise of the flow factor of this powder to the easy flowing range at 110° and 115 °C at lower consolidation stresses but keeps the free flowing range at higher stresses.

The outcomes obtained from the examination of powder flowability at elevated temperatures are consistent with the findings of earlier research studies for PA6, PA6black and PPNAT powders [35,36,68]. Changes in temperature can affect the crystal structure of materials, resulting in alterations to particle stiffness (a decrease in Young's modulus) and surface properties. These alterations can lead to visco-plastic deformation at the contact points between particles, increased adhesion, and greater interparticle force [69]. TPU powder does not show the same behaviour within the tested temperature range, even if the highest temperature adopted is only 5 °C below the initiation of melting. However, it is also true that changes in the flow properties are limited for all the powders below 110 °C as if the relevant properties to flowability were more related to the absolute temperature value rather than the temperature difference with the melting point.

3.2. Powder spreading assessment

3.2.1. Macroscopic images of powder bed surfaces

The macroscopic images of the surfaces of the prepared beds are reported in Figs. 8 to 11 for PA6, PA6 black, PPNAT and TPU in the

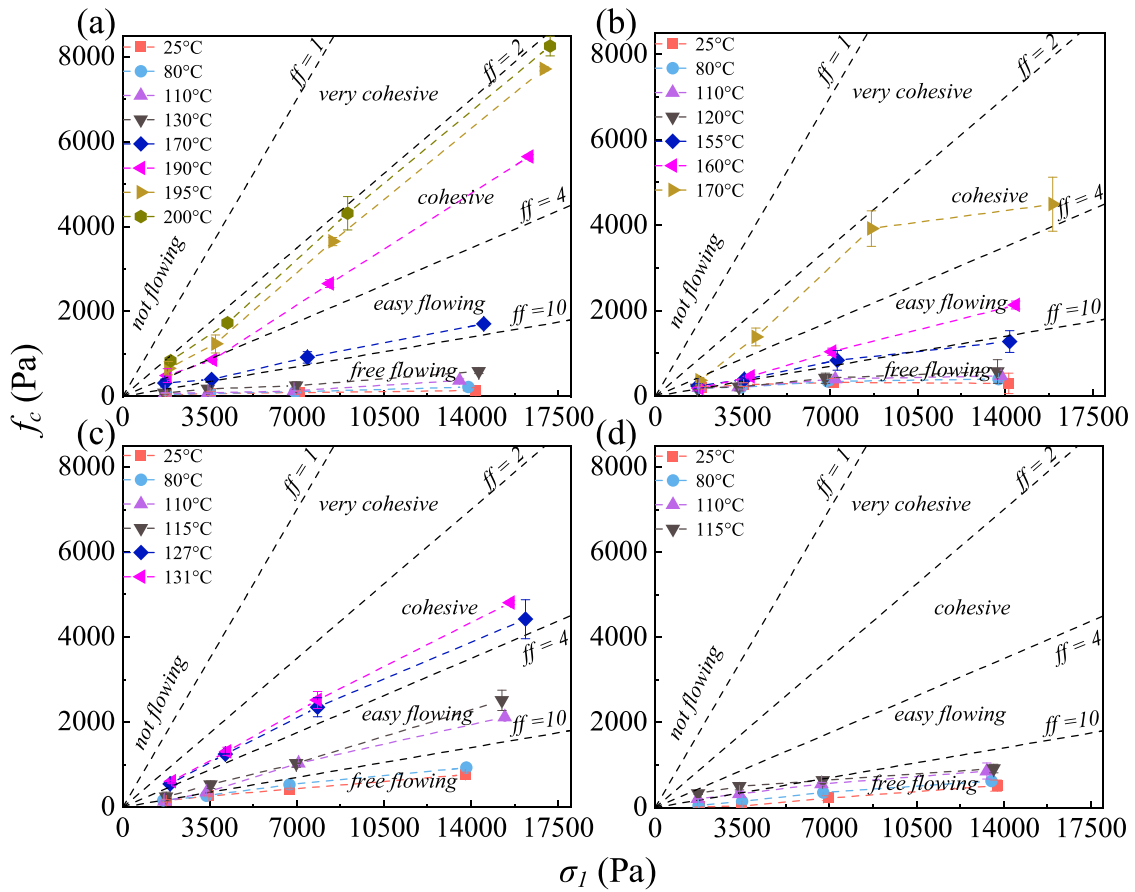


Fig. 7. Flow function graphs of powders at various temperatures: (a) PA6; (b) PA6 black; (c) PPNAT; (d) TPU.

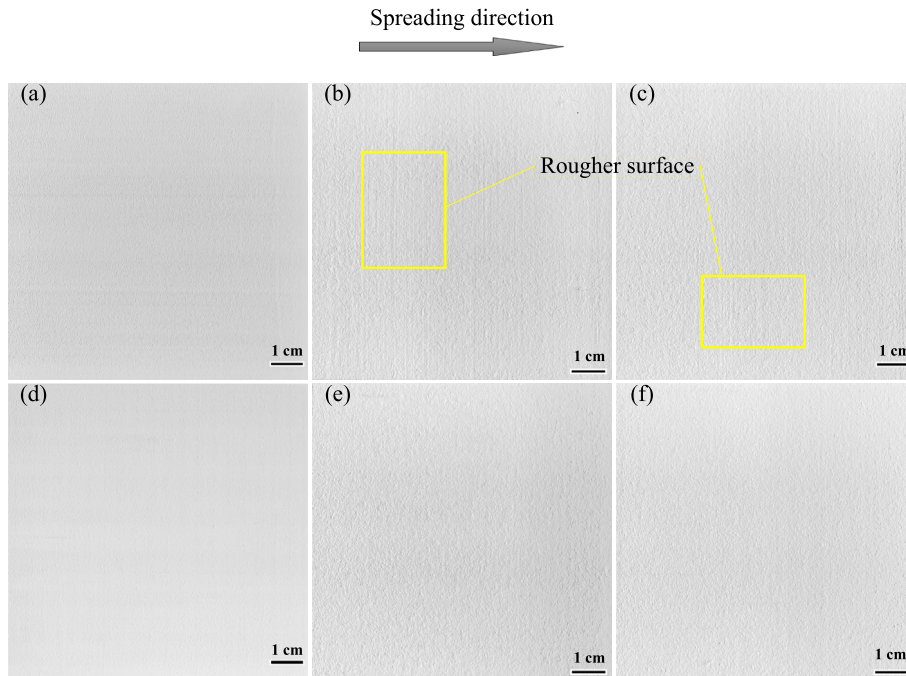


Fig. 8. Macroscopic images of PA6 powder captured from the powder fusing bed after completing the spreading process. At a spreading speed of 30 mm/s: (a) 25 °C; (b) 80 °C; (c) 110 °C. At a spreading speed of 3 mm/s: (d) 25 °C; (e) 80 °C; (f) 110 °C.

given order. In all these figures, panes a to c refer to experiments carried out at 25, 80 and 110 °C at 30 mm/s, and panes d to f refer to experiments carried out at 25, 80 and 110 °C at 3 mm/s.

Considering PA6 (Fig. 8), panes b and c for 30 mm/s of spreading speed at higher temperatures of 80 °C and 110 °C show some jagged marks (highlighted by yellow frames in the figure) on a

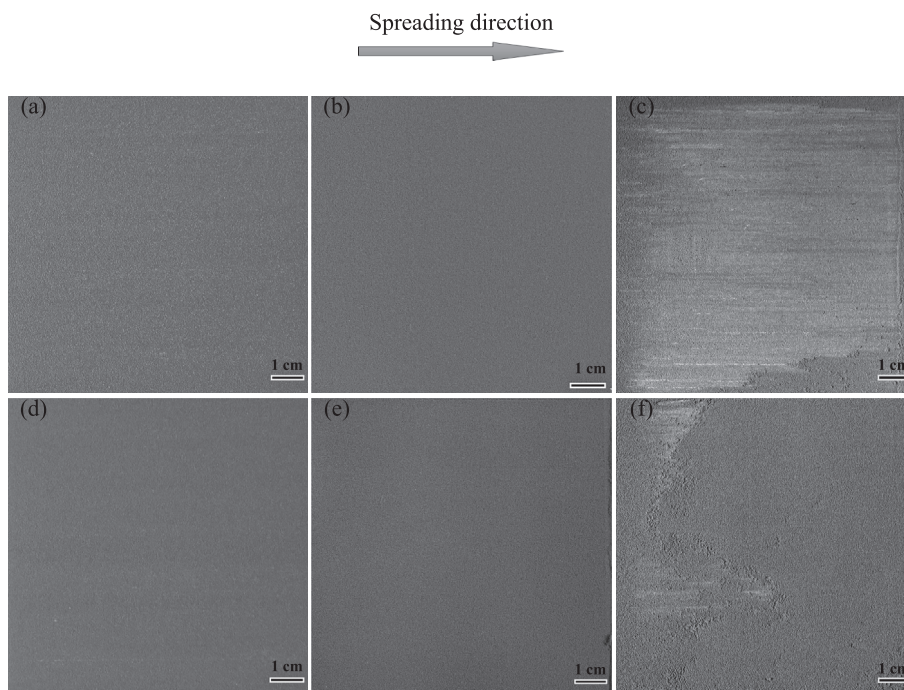


Fig. 9. Macroscopic images of PA6 black powder captured from the powder fusing bed after completing the spreading process. At a spreading speed of 30 mm/s: (a) 25 °C; (b) 80 °C; (c) 110 °C. At a spreading speed of 3 mm/s: (d) 25 °C; (e) 80 °C; (f) 110 °C.

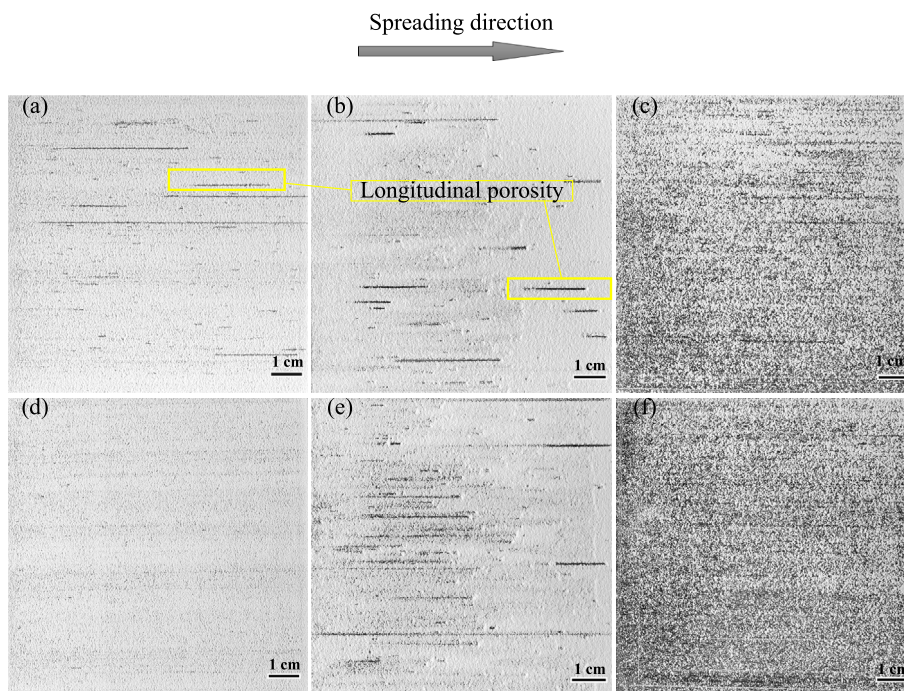


Fig. 10. Macroscopic images of PPNAT powder captured from the powder fusing bed after completing the spreading process. At a spreading speed of 30 mm/s: (a) 25 °C; (b) 80 °C; (c) 110 °C. At a spreading speed of 3 mm/s: (d) 25 °C; (e) 80 °C; (f) 110 °C.

slightly uneven surface texture, indicating a reduction of the surface quality compared to ambient temperature, not easily perceivable by direct visual inspection. The surface quality of the powder bed layer was less significantly affected by the temperature at a lower spreading speed of 3 mm/s (Fig. 8d–f). In general, however, the powder layer quality appears optimal.

From the macroscopic images of PA6 black at 25 °C and 80 °C (Fig. 9a–b and d–e), the visual inspection reveals that, at a spread-

ing speed of 30 mm/s, the layer quality improved moderately at increasing temperatures from 25 °C to 80 °C, less so at a spreading speed of 3 mm/s. PA6 black powder did not spread properly at 110 °C at both spreading speeds (Fig. 9c and f), resulting in a rough powder layer of poor quality.

For PPNAT powder at 30 mm/s spreading speed (Fig. 10a–c), the powder layer quality decreases at increasing temperature. For this material, the only satisfactory spreading condition is obtained at

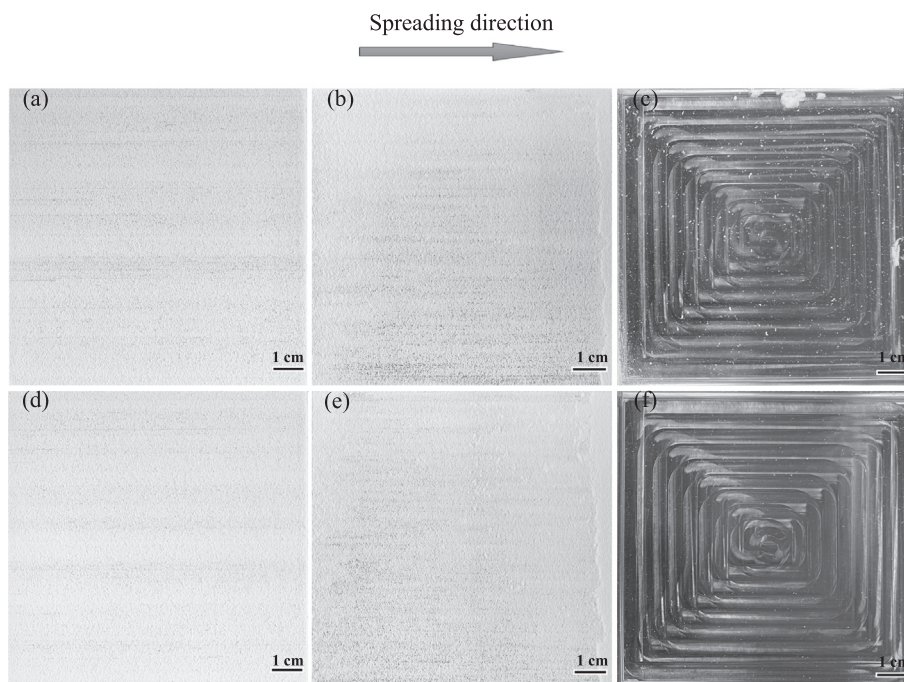


Fig. 11. Macroscopic images of TPU powder captured from the powder fusing bed after completing the spreading process. At a spreading speed of 30 mm/s: (a) 25 °C; (b) 80 °C; (c) 110 °C. At a spreading speed of 3 mm/s: (d) 25 °C; (e) 80 °C; (f) 110 °C.

25 °C and 3 mm/ spreading speed (Fig. 10d). However, the temperature also has a detrimental effect at this speed, showing the formation of longitudinal porosities at 80 °C highlighted by yellow frames in Fig. 10e. At 110 °C with both spreading speeds, the quality of the powder layer obtained is unacceptable (Fig. 10c and f).

TPU spread powder revealed a good spread powder layer at ambient temperature and 3 mm/s spreading speeds and a satisfactory spread layer at 30 mm/s and 80 °C for both spreading speeds. The behaviour of this powder changes abruptly at 110 °C. In fact, at this temperature, the powder did not spread at either spreading speed (Fig. 11 c and f), and the blade only swept the powder pile up without depositing particles due to the high cohesion.

Some of the binarised images of the powder layer using a threshold of 130 over a full range of grey levels between 0 (black) and 255 (white) are displayed in Fig. 12. A red border in the binary images marks the image limits. It appears that the threshold binarisation can catch the main surface defects for the bright powders. However, it must be noted that this procedure is able to highlight different kinds of defects, such as partial deposition of powder, powder agglomeration, and longitudinal porosities.

Table 2 provides results of the calculation of the experimental parameters evaluated from the images, namely the standard deviation of the grey level (SDG) for all the material and the irregularly or not covered fraction of the powder bed area (NCF) evaluated for the bright materials only, from binarised images. The same table also includes the perceived quality of the bed and a summary of the Jenike classification of the powder flow functions appearing in Fig. 7, considering the same temperatures used in the spreading tests. Inspection of the table indicates consistent ranges of SDG and NCF values for the different quality attributes of the bed and increasing values of both parameters in correspondence with decreasing bed quality. A summary of these ranges is given in Table 3. This table was obtained by looking at the SDG and NCF value ranges for each perceived bed quality attribute. Limiting values of SDG and NCF between adjacent attributes were obtained as an interpolation between the maximum available for the class of

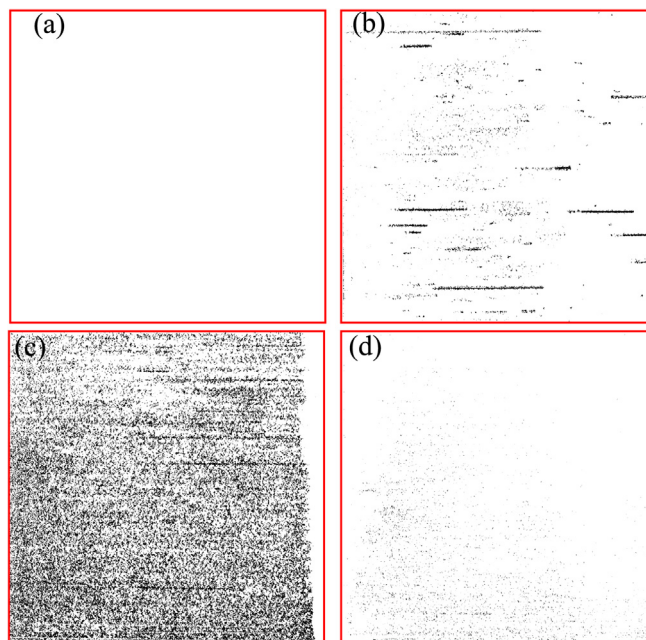


Fig. 12. Some of the binary images used to calculate the irregularly or not covered fraction of powder bed area (NCF): (a) PA6 at spreading speed 30 mm/s and 25 °C; (b) PPNAT at spreading speed 30 mm/s and 80 °C; (c) PPNAT at spreading speed 30 mm/s and 110 °C; (d) TPU at spreading speed 3 mm/s and 80 °C.

higher quality and the minimum available for the class of lower quality. Interestingly, while the SDG ranges span over a linear scale, NCF ranges map better on a logarithmic scale, indicating the larger sensitivity of the procedure using binarised images.

A summary of the powder layers' quality for the different materials at different temperatures and spreading velocities is reported in Fig. 13.

Table 2

The inspected quality of the layers and, obtained from the analysis of the macroscopic images, the standard deviation of the grey level (SDG) and irregularly or not covered fraction of powder bed area (NCF). The parameters NCF and SDG were calculated by analysing the macroscopic images. The table also reports the Jenike flowability of powders obtained from Fig. 7 from the flow functions measured at the spreading temperature.

Materials	Temperature (°C)	Spreading speed (mm/s)	NCF (%)	SDG	Spread powder quality	Powder Jenike Flowability
PA6	25	3	0.00	4.85	optimal	Free flowing
		30	0.00	8.66	optimal	
	80	3	0.00	11.38	optimal	Free flowing
		30	0.00	11.28	optimal	
	110	3	0.00	11.10	optimal	Free flowing
		30	0.00	12.57	optimal	
PA6 black	25	3	-	7.33	optimal	Free flowing
		30	-	8.08	optimal	
	80	3	-	14.31	optimal	Free flowing
		30	-	13.41	optimal	
	110	3	-	36.01	poor	Free flowing
		30	-	30.24	poor	
PPNAT	25	3	0.98	22.89	satisfactory	Free flowing
		30	2.80	27.11	poor	
	80	3	5.42	36.65	poor	Free flowing
		30	1.59	27.17	poor	
	110	3	38.60	72.38	unacceptable	Easy flowing
		30	27.41	68.85	unacceptable	
TPU	25	3	0.00	12.52	optimal	Free flowing
		30	0.13	17.63	satisfactory	
	80	3	0.79	20.57	satisfactory	Free flowing
		30	1.00	20.48	satisfactory	
	110	3	100.00	40.61	unacceptable	Free flowing
		30	100.00	40.15	unacceptable	

Table 3

The inspected quality and the corresponding ranges of NCF and SDG parameters.

Quality	NCF	SDG
optimal	<0.01 %	<15
satisfactory	0.01 % to 1 %	15 to 25
poor	1 % to 10 %	25 to 40
unacceptable	>10 %	>40

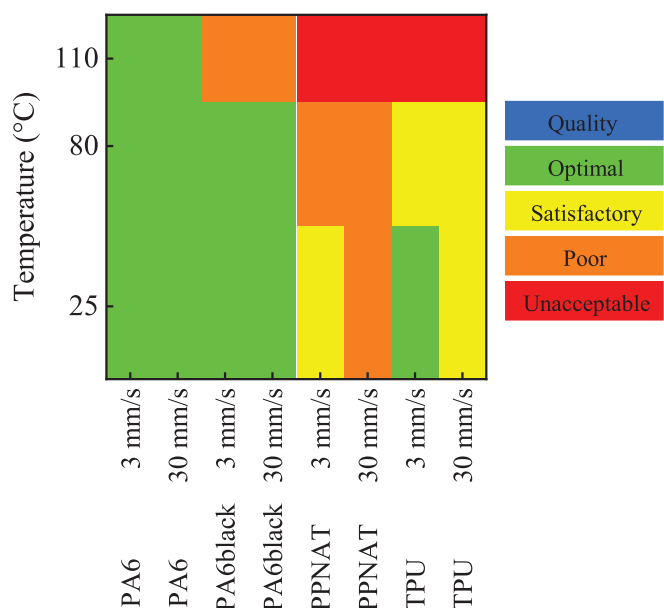


Fig. 13. Powder layer quality based on the direct visual inspection and the scales of image parameters NCF and SDG reported in Table 3.

3.2.2. Microscopic images of powder bed surfaces

Microscopic images of the powder bed surfaces are represented in Figs. 14 to 17 for PA6, PA6 Black, PPNAT and TPU. The figures

also report the power spectra of the wavelet analysis procedure described in section 2.4.2 above. Following Lupu et al. [31], the peak length, *pl*, is defined as the wavelength corresponding to the peak of the power spectrum.

For PA6, at 30 mm/s spreading speed and 25 °C (Fig. 14a), the powder layer shows a uniform surface with fine roughness that is characterised by wavy surface corrugations that are characterised by longer wavelengths. In the averaged wavelet power spectra extracted from these images (Fig. 14g), the indicated peak lengths shifted towards lower wave numbers corresponding to the larger characteristic wavelengths. The increasing width of power spectra exhibited at higher temperatures indicates a wider range of prevailing wavelengths, which indicates less uniform undulations, which do not necessarily correspond to a worse quality of the spread surface. At 3 mm/s, the effect of temperature is similar but with less marked impact on the surface quality, and the corresponding power spectra report more limited changes (Fig. 14d-f).

The microscopic images of PA6 black for this material reveal similar effects of temperature on the quality of the surface as those observed for PA6. In this case, with limited differences, both spreading speeds show increasingly larger, well-defined agglomerates in Fig. 15a to f. Coherently, in Fig. 15g to h, the power spectra of this material are moderately shifted towards larger wavelengths by increasing temperature and spreading speed. But, unlike PA6, the width of the power spectra is not significantly affected by temperature, an effect of the good definition of the surface agglomerates.

Fig. 16a to c and d to f report the microscopic images of PPNAT powder at increasing temperatures, and 30 mm/s and 3 mm/s, respectively, for the two series. Visual inspection indicates a change in powder layer quality from 25 °C to 80 °C towards smoother surfaces but overall more variable wavelengths. This variability is confirmed by wider wavelet power spectra in Fig. 16g to h, which also reveal an increase in the peak length. The powder layer quality is poor at 110 °C, where the spread layer is discontinuous, and the resulting power spectra confirm the temperature trends previously shown.

Fig. 17a to f show the microscopic images of the TPU powder. This powder spreads satisfactorily only at room temperature. How-

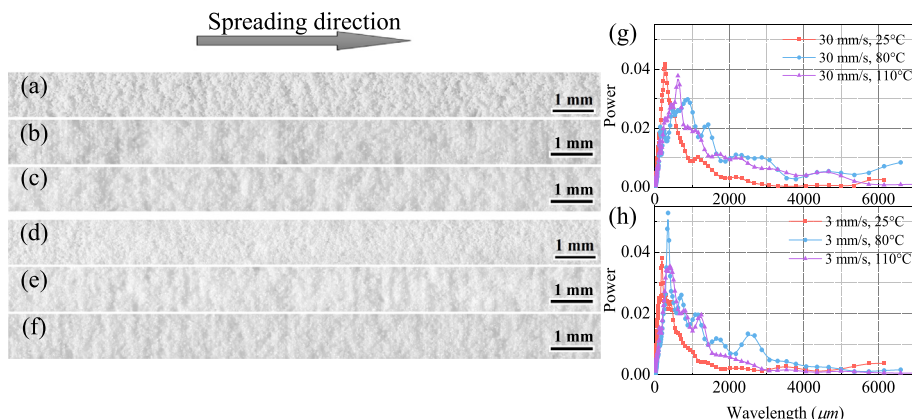


Fig. 14. Microscopic images of PA6 powder captured from the bed surface after completing the spreading process. At a spreading speed of 30 mm/s: (a) 25 °C; (b) 80 °C; (c) 110 °C. At a spreading speed of 3 mm/s: (d) 25 °C; (e) 80 °C; (f) 110 °C. Power spectra of the microscopic images taken from wavelet analysis: (g) 30 mm/s and (h) 3 mm/s.

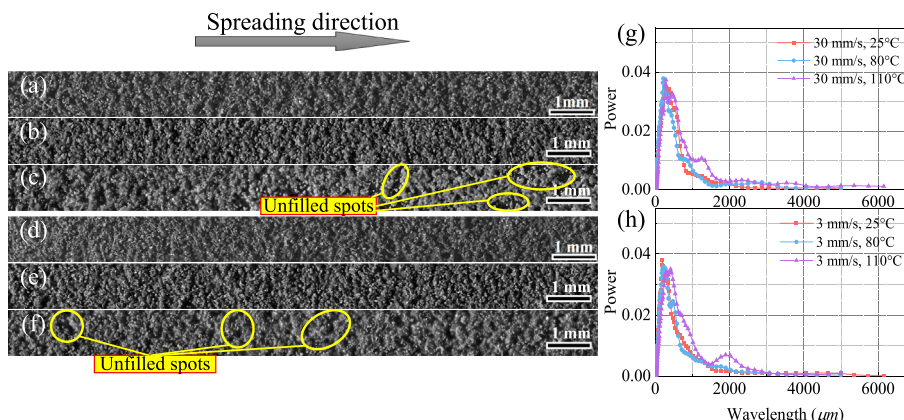


Fig. 15. Microscopic images of PA6 black powder captured from the bed surface after completing the spreading process. At a spreading speed of 30 mm/s: (a) 25 °C; (b) 80 °C; (c) 110 °C. At a spreading speed of 3 mm/s: (d) 25 °C; (e) 80 °C; (f) 110 °C. Power spectra of the microscopic images taken from wavelet analysis: (g) 30 mm/s and (h) 3 mm/s.

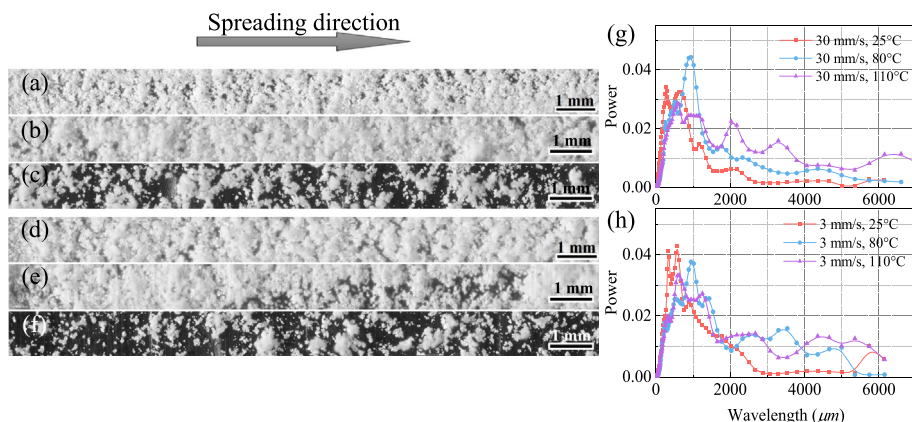


Fig. 16. Microscopic images of PPNAT powder captured from the bed surface after completing the spreading process. At a spreading speed of 30 mm/s: (a) 25 °C; (b) 80 °C; (c) 110 °C. At a spreading speed of 3 mm/s: (d) 25 °C; (e) 80 °C; (f) 110 °C. Power spectra of the microscopic images taken from wavelet analysis: (g) 30 mm/s and (h) 3 mm/s.

ever, the quality decreases at 80 °C for both spreading speeds, at which the layer appears agglomerated and discontinuous. The power spectra, however, reveal only small changes, indicating a similar size distribution of agglomerated powders (Fig. 17g and h). As previously mentioned, it was not possible to obtain any spread powder at 110 °C.

4. Discussion

The four materials tested are all polymer powders produced specifically for PBF-LB application at process temperatures higher than the range of the spreading process experiments carried out here. Therefore, it has to be assumed that all powders should

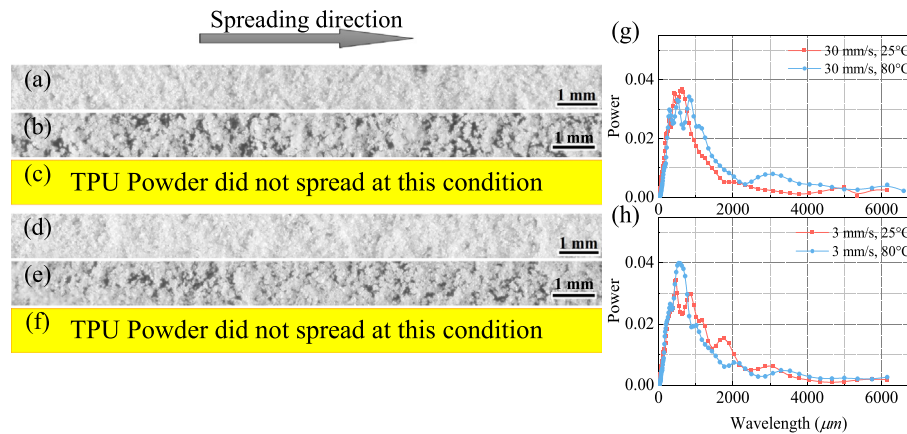


Fig. 17. Microscopic images of TPU powder captured from the bed surface after completing the spreading process. At a spreading speed of 30 mm/s: (a) 25 °C; (b) 80 °C; (c) 110 °C. At a spreading speed of 3 mm/s: (d) 25 °C; (e) 80 °C; (f) 110 °C. Power spectra of the microscopic images taken from wavelet analysis: (g) 30 mm/s and (h) 3 mm/s.

behave satisfactorily in the spreading process. Such behaviour is not found in the results of observations in the spreading process. So, this point requires a deeper analysis of the results.

From the point of view of particle size and particle size distributions (Fig. 2), the four materials are very similar, though PA6 shows slightly smaller particles while TPU shows larger particles. PA6 black and PPNAT instead have a narrower particle size distribution. Looking at spreadability results, none of these slightly changing properties can be directly related to spreadability results. Also, from the point of view of the particle shape, all these materials show angular particles, typical of mechanical particle comminution processes. The most significant difference between the powders staying in the constitutive material and the corresponding melting temperature (Fig. 4) is decreasing in the order PA6, PA6 black, PPNAT and TPU, in a range between 200 and 120 °C. Such range is well above the spreading temperatures tested that were included in the range between 25 and 110 °C. In this range, the powder flow function has only minor differences, perhaps more linked to possible capillary condensation that is out of control during the ambient temperature shear testing. Limiting the analysis to the ambient temperature, it seems encouraging that PPNAT, first and TPU, the second, are the materials which have the worst powder flowability (just slightly smaller flow factors in Fig. 7), and also shows, in the same order the poorest results in terms of macroscopic quality of the bed surface summarised in Fig. 13. Instead, the picture provided by wavelet power spectra of these materials is slightly less clear. Their power spectra are wider and show a larger peak length than PA6 and PA6 black. However, these features are not necessarily associated with worse quality layers comparing results at ambient temperature between these two materials.

Introducing the temperature effect on this analysis, the relationship between powder flowability and powder spreadability appears weak, as the flowability remains almost unchanged in the range below 110 °C, while significant changes are observed in the spreadability results relative to the surface quality. In this respect, the microscopic features revealed by the wavelet power spectra do not follow the strong changes evident in the macroscopic images.

Summarising, powder flowability and powder spreadability are only very weakly related, especially at process operating temperature. Other than the internal powder flow properties, some other system properties play a significant role in powder spreadability. The most likely is the interaction between the bed bottom and the particle in the spreading process. This interaction might also explain why powders showing bad behaviour in the spreading

experiment can be commonly used in the PBF process at the same temperature, as it was observed by Ruther et al. [38]. Comparing the results in this work and those by Ruther et al. [38], who carried out experiments on industrial setups in which the bed temperature is higher than that of the spread powder, it may be argued that such a temperature difference can play an important role. A deeper understanding of these phenomena would require a dedicated study. A possibility is to study the effect of changes in wall adhesion with temperature. Another possibility is to spread the powder layer over another one kept at a higher temperature.

5. Conclusions

This study focused on investigating the effect of temperature on flow properties and spreadability of polymeric powders to better understand their behaviour under high-temperature conditions in the PBF-LB process. The results are summarised below:

- An Anton Paar shear testing equipment was used to measure polymeric materials at high temperatures. Most of the outcomes align with previous findings regarding the impact of temperature. These can be clarified by an increase in van der Waals forces caused by a more pronounced plasticisation of the contact points as the temperature rises. In the range of temperatures used for the spreading test (25 to 110 °C), all the materials generally showed a very limited variability of the flow properties, which remained in the free-flowing range of the Jenike classification. The only exception was PPNAT. In fact, at 110 °C, this material showed a significant decrease in flowability, with the flow function falling in the easy-flowing range.
- During the testing of powders at varying temperatures, it was noticed that higher temperatures had an adverse effect on the spreadability of powders. This effect was particularly evident in the case of PPNAT and TPU powders, both of which have lower melting temperatures. However, the effect of temperature on the spreadability of PA6 powder was found to be relatively minor.
- A general lack of correlation was observed between powder flowability measured with shear tests and spreadability evaluated on the dedicated apparatus.
- The experimental process and image analysis procedure results can help quantitatively evaluate the quality of the layer surface produced during the spreading process at different temperatures.

- e) The method for classifying macroscopic images and detecting defects in powder layers can help assess overall quality under different spreading conditions.
- f) The averaged wavelet power spectra calculated on the grey level signal on microscopic panorama images can indicate the powder's local agglomeration tendency. However, this tendency is unrelated to the overall powder layer quality.
- g) Typically, the smoothness of the spread layer deteriorates as the spreading speed and temperature rise.
- h) A complete understanding of the spreading process requires a dedicated experiment considering the adequate interaction between the powder bed at the bottom of the spread layer and the powder spread by the spreading tool.

CRediT authorship contribution statement

Sina Zinatlou Ajabshir: Data curation, Formal Analysis, Investigation, Software, Visualization, Writing – original draft, Writing – review & editing. **Daniele Sofia:** Conceptualization, Data curation, Investigation, Resources, Software, Writing – original draft. **Colin Hare:** Conceptualization, Funding acquisition, Methodology, Supervision, Writing – original draft, Writing – review & editing. **Diego Barletta:** Conceptualization, Formal Analysis, Funding acquisition, Methodology, Supervision, Writing – original draft. **Massimo Poletto:** Conceptualization, Formal Analysis, Funding acquisition, Methodology, Project administration, Supervision, Writing – original draft, Writing – review & editing.

Declaration of Competing Interest

The authors declare that they have no known competing financial interests or personal relationships that could have appeared to influence the work reported in this paper.

Acknowledgements

Sina Zinatlou Ajabshir's research grant and part of the research were supported by MATHEGRAM. Marie SKŁODOWSKA-CURIE Innovative training network MATHEGRAM is funded through the People Programme (Marie SKŁODOWSKA-CURIE Actions) of the European Union's Horizon 2020 Programme H2020 under REA grant agreement No. 813202.

References

- [1] ISO/ASTM 52900:2021(en), Additive manufacturing – General principles – Fundamentals and vocabulary, (n.d.).
- [2] A.T. Sutton, C.S. Kriewall, M.C. Leu, J.W. Newkirk, Powder characterisation techniques and effects of powder characteristics on part properties in powder-bed fusion processes, *Virtual Phys. Prototyp.* 12 (2017), <https://doi.org/10.1080/17452759.2016.1250605>.
- [3] M. Tang, P.C. Pistorius, J.L. Beuth, Prediction of lack-of-fusion porosity for powder bed fusion, *Addit. Manuf.* 14 (2017), <https://doi.org/10.1016/j.addma.2016.12.001>.
- [4] J.L. Bartlett, X. Li, An overview of residual stresses in metal powder bed fusion, *Addit. Manuf.* 27 (2019), <https://doi.org/10.1016/j.addma.2019.02.020>.
- [5] C.R. Deckard, Method and apparatus for producing parts by selective sintering, United States Patent No. 4,863,538 (1986).
- [6] C.R. Deckard, J.J. Beaman, J.F. Darrach, Method for selective laser sintering with layerwise cross-scanning, United States Patent No. 5,155,324 (1990).
- [7] C.R. Deckard, Apparatus for producing parts by selective sintering, United States Patent No. 5,597,589 (1994).
- [8] I.A. Manriquez-Frayre, D.L. Bourell, Selective Laser Sintering of Binary Metallic Powder (1990) 99–106.
- [9] Y.P. Kathuria, Microstructuring by selective laser sintering of metallic powder, *Surf. Coatings Technol.* 116–119 (1999) 643–647, [https://doi.org/10.1016/S0257-8972\(99\)00266-2](https://doi.org/10.1016/S0257-8972(99)00266-2).
- [10] R. Glardon, N. Karapatis, V. Romano, Influence of nd: YAG parameters on the selective laser sintering of metallic powders, *CIRP Ann. - Manuf. Technol.* 50 (2001) 133–136, [https://doi.org/10.1016/S0007-8506\(07\)62088-5](https://doi.org/10.1016/S0007-8506(07)62088-5).
- [11] X.C. Wang, T. Laoui, J. Bonse, J.P. Kruth, B. Lauwers, L. Froyen, Direct selective laser sintering of hard metal powders: Experimental study and simulation, *Int. J. Adv. Manuf. Technol.* 19 (2002) 351–357, <https://doi.org/10.1007/s001700200024>.

- [12] M.A. Eryomina, S.F. Lomayeva, E.V. Kharanzhevsky, V.V. Tarasov, I.N. Burnyshev, Wet ball milling and subsequent high-speed selective laser sintering of Nb–Cu powders for applying wear-resistant coatings, *Int. J. Refract. Met. Hard Mater.* 105 (2022) 105837, <https://doi.org/10.1016/j.ijrmhm.2022.105837>.
- [13] D. Sofia, R. Chirone, P. Lettieri, D. Barletta, M. Poletto, Selective laser sintering of ceramic powders with bimodal particle size distribution, *Chem. Eng. Res. Des.* 136 (2018) 536–547, <https://doi.org/10.1016/j.cherd.2018.06.008>.
- [14] A.B. Peters, D. Zhang, A. Hernandez, M.C. Brupbacher, D.C. Nagle, T. Mueller, J.B. Spicer, Selective laser sintering in reactive atmospheres: Towards in-situ synthesis of net-shaped carbide and nitride ceramics, *Addit. Manuf.* 45 (2021) 102052, <https://doi.org/10.1016/j.addma.2021.102052>.
- [15] W. Zheng, J.M. Wu, S. Chen, K.B. Yu, J. Zhang, H. Liu, S.F. Wen, C.Z. Yan, Y.S. Shi, Preparation of high-performance silica-based ceramic cores with B4C addition using selective laser sintering and SiO₂–Al₂O₃ sol infiltration, *Ceram. Int.* 49 (2023) 6620–6629, <https://doi.org/10.1016/j.ceramint.2022.10.147>.
- [16] M.B. Sagar, K. Elangovan, Consolidation & factors influencing sintering process in polymer powder based additive manufacturing, *IOP Conf. Ser. Mater. Sci. Eng.* 225 (2017), <https://doi.org/10.1088/1757-899X/225/1/012075>.
- [17] L.J. Tan, W. Zhu, K. Sagar, K. Zhou, Comparative study on the selective laser sintering of polypropylene homopolymer and copolymer: processability, crystallisation kinetics, crystal phases and mechanical properties, *Addit. Manuf.* 37 (2021) 101610, <https://doi.org/10.1016/j.addma.2020.101610>.
- [18] D. Soldner, S. Greiner, C. Burkhardt, D. Drummer, P. Steinmann, J. Mergheim, Numerical and experimental investigation of the isothermal assumption in selective laser sintering of PA12, *Addit. Manuf.* 37 (2021) 101676, <https://doi.org/10.1016/j.addma.2020.101676>.
- [19] P. Hejmady, L.C.A. van Breemen, D. Hermida-Merino, P.D. Anderson, R. Cardinaels, Laser sintering of PA12 particles studied by in-situ optical, thermal and X-ray characterisation, *Addit. Manuf.* 52 (2022) 102624, <https://doi.org/10.1016/j.addma.2022.102624>.
- [20] A. El Magri, S.E. Bencaid, H.R. Vanaei, S. Vaudreuil, Effects of laser power and hatch orientation on final properties of PA12 Parts produced by selective laser sintering, *Polymers (basel)*, 14 (2022), <https://doi.org/10.3390/polym14173674>.
- [21] C. Gómez-Rodríguez, L.V. García-Quiñonez, L.F. Verdeja, G.A. Castillo-Rodríguez, J.A. Aguilar-Martínez, A.E. Mariño-Gómez, D. Fernández-González, Selective laser sintering of alumina-molybdenum nanocomposites, *Ceram. Int.* 48 (2022) 29540–29545, <https://doi.org/10.1016/j.ceramint.2022.08.058>.
- [22] M. Zhou, W. Zhu, S. Yu, Y. Tian, K. Zhou, Selective laser sintering of carbon nanotube-coated thermoplastic polyurethane: mechanical, electrical, and piezoresistive properties, *Compos. Part C Open Access*, 7 (2022) 100212, <https://doi.org/10.1016/j.jcom.2021.100212>.
- [23] S. Yu, T. Zeng, J. Zhao, H. Jiang, Z. Chen, Y. Yang, Z. Zhong, S. Cheng, Preparation and electromagnetic wave absorption properties of PDC–SiC/Si₃N₄ composites using selective laser sintering and infiltration technology, *J. Mater. Res. Technol.* (2023), <https://doi.org/10.1016/j.jmrt.2023.01.202>.
- [24] K. Deng, H. Wu, Y. Li, J. Jiang, M. Wang, Z. Yang, R. Zhang, The resin-ceramic-based Fe₃O₄/graphite composites rapidly fabricated by selective laser sintering for integration of structural-bearing and broadband electromagnetic wave absorption, *J. Alloys Compd.* 943 (2023) 169120, <https://doi.org/10.1016/j.jallcom.2023.169120>.
- [25] Y. Fu, C. Yan, X. Yang, Z. Liu, P. Chen, Z. Li, Preparation and Selective Laser Sintering of Nylon-12 Coated Copper Powders 7 (2021) 1355–1362, <https://doi.org/10.1108/RPJ-06-2020-0131>.
- [26] L.I. Escano, N.D. Parab, L. Xiong, Q. Guo, C. Zhao, K. Fezzaa, W. Everhart, T. Sun, L. Chen, Revealing particle-scale powder spreading dynamics in powder-bed-based additive manufacturing process by high-speed x-ray imaging, *Sci. Rep.* 8 (2018) 1–11, <https://doi.org/10.1038/s41598-018-33376-0>.
- [27] C. Meier, R. Weissbach, W.A. Wall, Critical influences of Particle size and adhesion on the powder layer uniformity in metal additive Manufacturing, *J. Mater. Process. Technol.* (2018), <https://doi.org/10.1016/j.jmatprotec.2018.10.037>.
- [28] L. Cordova, T. Bor, M. de Smit, M. Campos, T. Tinga, Measuring the spreadability of pre-treated and moisturised powders for laser powder bed fusion, *Addit. Manuf.* 32 (2020) 101082, <https://doi.org/10.1016/j.addma.2020.101082>.
- [29] Y. He, A. Hassanpour, A.E. Bayly, Combined effect of particle size and surface cohesiveness on powder spreadability for additive manufacturing, *Powder Technol.* 392 (2021) 191–203, <https://doi.org/10.1016/j.powtec.2021.06.046>.
- [30] M. Mehrabi, J. Gardy, F.A. Talebi, A. Farshchi, A. Hassanpour, A.E. Bayly, An investigation of the effect of powder flowability on the powder spreading in additive manufacturing, *Powder Technol.* 413 (2023) 117997, <https://doi.org/10.1016/j.powtec.2022.117997>.
- [31] M. Lupo, S. Zinatlou Ajabshir, D. Sofia, D. Barletta, M. Poletto, Experimental metrics of the powder layer quality in the selective laser sintering process, *Powder Technol.* 419 (2023) 118346, <https://doi.org/10.1016/j.powtec.2023.118346>.
- [32] S. Yim, H. Bian, K. Aoyagi, K. Yamanaka, A. Chiba, Spreading behavior of Ti–48Al–2Cr–2Nb powders in powder bed fusion additive manufacturing process: Experimental and discrete element method study, *Addit. Manuf.* 49 (2022) 102489, <https://doi.org/10.1016/j.addma.2021.102489>.

- [33] Y. Zhao, J.W. Chew, Effect of lognormal particle size distributions on particle spreading in additive manufacturing, *Adv. Powder Technol.* 32 (2021), <https://doi.org/10.1016/j.apt.2021.02.019>.
- [34] D. Yao, J. Wang, M. Li, T. Zhao, Y. Cai, X. An, R. Zou, H. Zhang, H. Fu, X. Yang, Q. Zou, Segregation of 316L stainless steel powder during spreading in selective laser melting based additive manufacturing, *Powder Technol.* 397 (2022) 117096, <https://doi.org/10.1016/j.powtec.2021.117096>.
- [35] D. Ruggi, C. Barrès, J.Y. Charneau, R. Fulchiron, D. Barletta, M. Poletto, A quantitative approach to assess high temperature flow properties of a PA 12 powder for laser sintering, *Addit. Manuf.* 33 (2020) 101143, <https://doi.org/10.1016/j.addma.2020.101143>.
- [36] D. Ruggi, M. Lupo, D. Sofia, C. Barrès, D. Barletta, M. Poletto, Flow properties of polymeric powders for selective laser sintering, *Powder Technol.* 370 (2020) 288–297, <https://doi.org/10.1016/j.powtec.2020.05.069>.
- [37] S. Zinatlou Ajabshir, C. Hare, D. Sofia, D. Barletta, M. Poletto, Investigating the effect of temperature on powder spreading behaviour in powder bed fusion additive manufacturing process by discrete element method, *Powder Technol.* 436 (2024) 119468, <https://doi.org/10.1016/j.powtec.2024.119468>.
- [38] M. Rütther, S.H. Klippstein, S.K. Ponusamy, T. Rütther, H.J. Schmid, Flowability of polymer powders at elevated temperatures for additive manufacturing, *Powder Technol.* 422 (2023), <https://doi.org/10.1016/j.powtec.2023.118460>.
- [39] M. Horn, M. Schmitt, L. Langer, G. Schlick, C. Seidel, Laser powder bed fusion recoater selection guide – Comparison of resulting powder bed properties and part quality, *Powder Technol.* 434 (2024) 119356, <https://doi.org/10.1016/j.powtec.2023.119356>.
- [40] A. Phua, C. Doblin, P. Owen, C.H.J. Davies, G.W. Delaney, The effect of recoater geometry and speed on granular convection and size segregation in powder bed fusion, *Powder Technol.* 394 (2021), <https://doi.org/10.1016/j.powtec.2021.08.058>.
- [41] M. Schmidt, D. Pohle, T. Rechtenwald, Selective laser sintering of PEEK, *CIRP Ann. - Manuf. Technol.* 56 (2007) 205–208, <https://doi.org/10.1016/j.cirp.2007.05.097>.
- [42] Q. Liu, Y. Danlos, B. Song, B. Zhang, S. Yin, H. Liao, Effect of high-temperature preheating on the selective laser melting of yttria-stabilised zirconia ceramic, *J. Mater. Process. Technol.* 222 (2015) 61–74, <https://doi.org/10.1016/j.jmatprotec.2015.02.036>.
- [43] R. Mertens, S. Dadbakhsh, J. Van Humbeeck, J.P. Kruth, Application of base plate preheating during selective laser melting, *Procedia CIRP.* 74 (2018) 5–11, <https://doi.org/10.1016/j.procir.2018.08.002>.
- [44] X. Zhang, F. Wang, Z. Wu, M. Nastasi, Y. Chen, Y. Hao, Direct selective laser sintering of hexagonal barium titanate ceramics, *J. Am. Ceram. Soc.* 104 (2021) 1271–1280, <https://doi.org/10.1111/jace.17568>.
- [45] H.S. Maurya, L. Kollo, K. Juhani, F. Sergejev, K.G. Prashanth, Effect of preheating and cooling of the powder bed by laser pulse shaping on the microstructure of the TiC based cermets, *Ceram. Int.* 48 (2022) 20612–20618, <https://doi.org/10.1016/j.ceramint.2022.04.029>.
- [46] S. Waqar, K. Guo, J. Sun, Evolution of residual stress behavior in selective laser melting (SLM) of 316L stainless steel through preheating and in-situ rescanning techniques, *Opt. Laser Technol.* 149 (2022) 107806, <https://doi.org/10.1016/j.optlastec.2021.107806>.
- [47] L. Zhou, J. Sun, J. Chen, W. Chen, Y. Ren, Y. Niu, C. Li, W. Qiu, Study of substrate preheating on the microstructure and mechanical performance of ti-15Mo alloy processed by selective laser melting, *J. Alloys Compd.* 928 (2022) 167130, <https://doi.org/10.1016/j.jallcom.2022.167130>.
- [48] Z. Yang, X. Liu, Z. Zhang, S. Li, Q. Fang, Analysis of preheating temperature field characteristics in selective laser sintering, *Adv. Mech. Eng.* 14 (2022) 1–14, <https://doi.org/10.1177/16878140211072397>.
- [49] A.I.B. Idriss, J. Li, Y. Guo, E.A. Elfaki, Sintering quality and parameters optimisation of sisal fiber / PES composite fabricated by selective laser sintering (SLS), *J. Thermoplast. Compos. Mater.* 35 (2022) 1632–1646, <https://doi.org/10.1177/0892705720939179>.
- [50] K. Shahzad, J. Deckers, J.P. Kruth, J. Vleugels, Additive manufacturing of alumina parts by indirect selective laser sintering and post processing, *J. Mater. Process. Technol.* 213 (2013) 1484–1494, <https://doi.org/10.1016/j.jmatprotec.2013.03.014>.
- [51] B. Qian, Z. Shen, Laser sintering of ceramics, *J. Asian Ceram. Soc.* (2013), <https://doi.org/10.1016/j.jascer.2013.08.004>.
- [52] K. Kempen, L. Thijs, B. Vrancken, S. Buls, J. Van Humbeeck, J.P. Kruth, Producing crack-free, high density M2 HSS parts by Selective Laser Melting: Preheating the baseplate, in: 24th Int. SFF Symp. - An Addit. Manuf. Conf. SFF, 2013: pp. 131–139.
- [53] L. Facchini, E. Magalini, P. Robotti, A. Molinari, S. Höges, K. Wissenbach, Ductility of a ti-6Al-4V alloy produced by selective laser melting of prealloyed powders, *Rapid Prototyp. J.* 16 (2010) 450–459, <https://doi.org/10.1108/13552541011083371>.
- [54] J.P. Kruth, L. Froyen, M. Rombouts, J. Van Vaerenbergh, P. Mercelis, New ferro powder for selective laser sintering of dense parts, *CIRP Ann. - Manuf. Technol.* 52 (2003) 139–142, [https://doi.org/10.1016/S0007-8506\(07\)60550-2](https://doi.org/10.1016/S0007-8506(07)60550-2).
- [55] I. Yadroitsev, P. Krakhmalev, I. Yadroitsava, S. Johansson, I. Smurov, Energy input effect on morphology and microstructure of selective laser melting single track from metallic powder, *J. Mater. Process. Technol.* 213 (2013) 606–613, <https://doi.org/10.1016/j.jmatprotec.2012.11.014>.
- [56] Y. Tang, J.Y.H. Fuh, H.T. Loh, Y.S. Wong, L. Lu, Direct laser sintering of a silica sand, *Mater. Des.* 24 (2003) 623–629, [https://doi.org/10.1016/S0261-3069\(03\)00126-2](https://doi.org/10.1016/S0261-3069(03)00126-2).
- [57] P. Bertrand, F. Bayle, C. Combe, P. Goeuriot, I. Smurov, Ceramic components manufacturing by selective laser sintering, *Appl. Surf. Sci.* 254 (2007) 989–992, <https://doi.org/10.1016/j.apsusc.2007.08.085>.
- [58] H. Chung, S. Das, Processing and properties of glass bead particulate-filled functionally graded Nylon-11 composites produced by selective laser sintering, *Mater. Sci. Eng. a.* 437 (2006) 226–234, <https://doi.org/10.1016/j.msea.2006.07.112>.
- [59] M. Van den Eynde, L. Verbelen, P. Van Puyvelde, Assessing polymer powder flow for the application of laser sintering, *Powder Technol.* 286 (2015) 151–155, <https://doi.org/10.1016/j.powtec.2015.08.004>.
- [60] W. Nan, Y. Gu, Experimental investigation on the spreadability of cohesive and frictional powder, *Adv. Powder Technol.* 33 (2022) 103466, <https://doi.org/10.1016/j.apt.2022.103466>.
- [61] M. Ahmed, M. Pasha, W. Nan, M. Ghadiri, A simple method for assessing powder spreadability for additive manufacturing, *Powder Technol.* 367 (2020) 671–679, doi:10.1016/j.powtec.2020.04.033.
- [62] A. Mussatto, R. Groarke, A.O. Neill, M. Ahmed, Y. Delaure, D. Brabazon, Influences of powder morphology and spreading parameters on the powder bed topography uniformity in powder bed fusion metal additive manufacturing, *Addit. Manuf.* 38 (2021) 101807, <https://doi.org/10.1016/j.addma.2020.101807>.
- [63] H. Salehi, J. Cummins, E. Gallino, N. Harrison, A. Hassanpour, M. Bradley, A new approach to quantify powder's bed surface roughness in additive manufacturing, *Powder Technol.* 407 (2022) 117614, <https://doi.org/10.1016/j.powtec.2022.117614>.
- [64] H. Salehi, D. Sofia, D. Schütz, D. Barletta, M. Poletto, Experiments and simulation of torque in Anton Paar powder cell, *Part. Sci. Technol.* 36 (2018) 501–512, <https://doi.org/10.1002/aic.15934>.
- [65] S. Yim, K. Aoyagi, H. Bian, Y. Cui, A. Chiba, Factors determining the flowability and spreading quality of gas-atomised ti-48Al-2Cr-2Nb powders in powder bed fusion additive manufacturing, *Powder Technol.* 412 (2022) 117996, <https://doi.org/10.1016/j.powtec.2022.117996>.
- [66] R.D. Goodridge, C.J. Tuck, R.J.M. Hague, Laser sintering of polyamides and other polymers, *Prog. Mater. Sci.* 57 (2012) 229–267, <https://doi.org/10.1016/j.pmatsci.2011.04.001>.
- [67] S. Berretta, O. Ghita, K.E. Evans, Morphology of polymeric powders in laser sintering (LS): from polyamide to new PEEK powders, *Eur. Polym. J.* 59 (2014), <https://doi.org/10.1016/j.eurpolymj.2014.08.004>.
- [68] S. Zinatlou Ajabshir, C. Gucuyener, V. Vivacqua, D. Gobby, H. Stitt, D. Barletta, M. Poletto, Flow behaviour of zeolite powders at high process temperatures, *Powder Technol.* 409 (2022) 117818, <https://doi.org/10.1016/j.powtec.2022.117818>.
- [69] M. Ripp, S. Ripperger, Influence of temperature on the flow properties of bulk solids, *Chem. Eng. Sci.* 65 (2010) 4007–4013, <https://doi.org/10.1016/j.ces.2010.03.046>.